# Crystal structures and atomic model of NADPH oxidase

Magnani, Francesca; Nenci, Simone; Fananas, Elisa Millana; Ceccon, Marta; Romero, Elvira; Fraaije, Marco W.; Mattevi, Andrea

*Published in:*
Proceedings of the National Academy of Science of the United States of America

*DOI:*
10.1073/pnas.1702293114



*Publication date:*
2017

# Crystal structures and atomic model of NADPH oxidase

Francesca Magnani[a,1,2], Simone Nenci[a,1], Elisa Millana Fananas[a], Marta Ceccon[a], Elvira Romero[b], Marco W. Fraaije[b], and Andrea Mattevi[a,2]

[a]Department of Biology and Biotechnology "L. Spallanzani," University of Pavia, 27100 Pavia, Italy; and [b]Molecular Enzymology Group, University of Groningen, 9747 AG Groningen, The Netherlands

Edited by Carl F. Nathan, Weill Medical College of Cornell University, New York, NY, and approved May 16, 2017 (received for review February 9, 2017)

**NADPH oxidases (NOXs) are the only enzymes exclusively dedicated to reactive oxygen species (ROS) generation. Dysregulation of these polytopic membrane proteins impacts the redox signaling cascades that control cell proliferation and death. We describe the atomic crystal structures of the catalytic flavin adenine dinucleotide (FAD)- and heme-binding domains of *Cylindrospermum stagnale* NOX5. The two domains form the core subunit that is common to all seven members of the NOX family. The domain structures were then docked in silico to provide a generic model for the NOX family. A linear arrangement of cofactors (NADPH, FAD, and two membrane-embedded heme moieties) injects electrons from the intracellular side across the membrane to a specific oxygen-binding cavity on the extracytoplasmic side. The overall spatial organization of critical interactions is revealed between the intracellular loops on the transmembrane domain and the NADPH-oxidizing dehydrogenase domain. In particular, the C terminus functions as a toggle switch, which affects access of the NADPH substrate to the enzyme. The essence of this mechanistic model is that the regulatory cues conformationally gate NADPH-binding, implicitly providing a handle for activating/deactivating the very first step in the redox chain. Such insight provides a framework to the discovery of much needed drugs that selectively target the distinct members of the NOX family and interfere with ROS signaling.**

membrane protein | reactive oxygen species | oxidative stress | redox biology | NOX

The NADPH-oxidases (NOXs) form the only known enzyme family whose sole function is reactive oxygen species (ROS) generation (1, 2). Initially described in mammalian phagocytes and called phagocyte oxidases, NOXs were shown to function as "bacterial killers" through the production of bactericidal oxygen species using molecular oxygen and NADPH as substrates. The importance of the phagocyte oxidase (now known as NOX2) in host defense was demonstrated by the severe infections that occur in patients affected by chronic granulomatous disease, in which the phagocytes suffer by inefficient superoxide-producing NOX activities (3). After this initial discovery, it was found that mammals contain several enzyme isoforms: NOX1–5 and Duox1–2, which differ with respect to their specific activities and tissue distribution (2). Each of these seven human NOXs is finely regulated by protein–protein interactions and signaling molecules to be activated only after the proper physiological stimuli. Consistently, NOXs are typically associated to cytosolic protein partners, which can switch on/off the oxidase activity. It has now become clear that NOXs primarily function as key players in cell differentiation, senescence, and apoptosis (4–8). Of note, oncogene expression has been widely reported to depend upon ROS production to exert its mitogenic effects and NOX1/4 are emerging as attractive targets for anticancer chemo-therapeutics (9–11). Pharmacological intervention on NOXs, which is intensively sought against inflammatory and oncology diseases, is currently hampered by the lack of selective drugs (12).

NOXs are membrane proteins that share the same catalytic core: a six transmembrane helical domain (TM) and a C-terminal cytosolic dehydrogenase domain (DH). DH contains the binding sites for FAD (flavin adenine dinucleotide) and NADPH, whereas TM binds two hemes (1, 2, 13). The enzyme catalytic cycle entails a series of steps, which sequentially transfer electrons from cytosolic NADPH to an oxygen-reducing center located on the extracytoplasmic side of the membrane (hereafter referred to as the "outer side"). Thus, a distinctive feature of NOXs is that NADPH oxidation and ROS production take place on the opposite sides of the membrane (1, 2). The main obstacle to the structural and mechanistic investigation of NOX's catalysis and regulation has been the difficulty encountered with obtaining well-behaved proteins in sufficient amounts. In fact, the overexpression of NOXs is often toxic to cells, with consequent loss of biomass and final protein yield. Moreover, upon extraction from the membranes, these enzymes tend to proteolyze spontaneously and lose their noncovalently bound cofactors (FAD and hemes). Therefore, a different approach had to be devised to achieve a crystallizable protein. We reasoned that the single-subunit NOX5 could be an attractive system for structural studies because it does not require accessory proteins for its function, which is instead regulated by an N-terminal calcium-binding EF-hand domain (Fig. S1*A*) (14, 15). Several eukaryotic and prokaryotic NOX5 orthologs were investigated for recombinant protein expression and stability. We found *Cylindrospermum stagnale* NOX5 (csNOX5) to be promising for structural studies. csNOX5 bears a very significant 40% sequence identity to human NOX5 and was likely acquired by cyanobacteria through gene transfer from a higher eukaryote (Fig. S1*B*) (14). To overcome proteolysis issues presented by the full-length csNOX5, we adopted a "divide and conquer" approach and proceeded to work on the individual domains. Here,

## Significance

**Reactive oxygen species (ROS) are far from being only an inevitable byproduct of respiration. They are instead actively generated by NADPH oxidases (NOXs), a family of highly regulated enzymes that underpin complex functions in the control of cell proliferation and antibacterial defense. By investigating the individual catalytic domains, we elucidate the core of the NOX 3D structure. An array of cofactors is spatially organized to transfer reducing electrons from the intracellular milieu to the ROS-generating site, exposed to the outer side of the cell membrane. This redox chain is finely tuned by structural elements that cooperate to control NADPH binding, thereby preventing noxious spills of ROS. Our findings indicate avenues for the pharmacological manipulation of NOX activity.**

Author contributions: F.M., S.N., and A.M. designed research; F.M., S.N., E.M.F., M.C., E.R., and M.W.F. performed research; F.M., S.N., E.M.F., M.C., E.R., M.W.F., and A.M. analyzed data; and F.M., S.N., and A.M. wrote the paper.

The authors declare no conflict of interest.

This article is a PNAS Direct Submission.

Data deposition: The atomic coordinates have been deposited in the Protein Data Bank, www.pdb.org [transmembrane domain (PDB ID code 5O0T) and dehydrogenase domain (PDB ID code 5O0X)].

[1]F.M. and S.N. contributed equally to this work.

[2]To whom correspondence may be addressed. Email: francesca.magnani@unipv.it or andrea.mattevi@unipv.it.

This article contains supporting information online at www.pnas.org/lookup/suppl/doi:10.1073/pnas.1702293114/-/DCSupplemental.

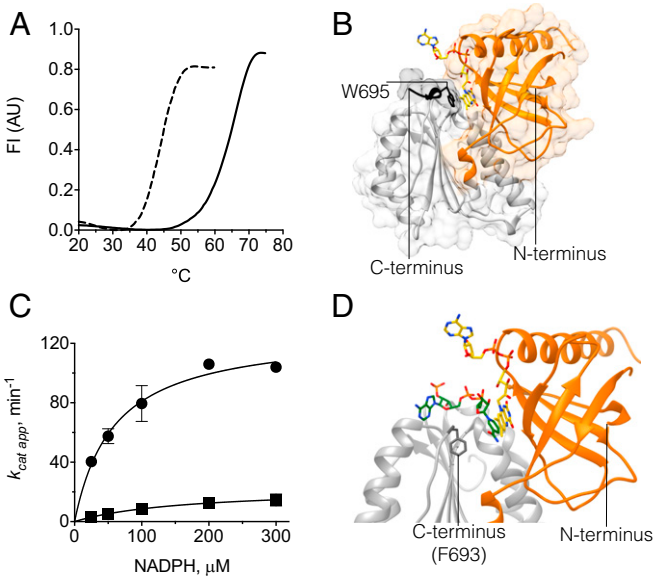


**Fig. 1.** Characterization of the mutant csDH domain and its structure in complex with FAD. (*A*) Thermal denaturation curves demonstrate higher stability of the mutant csDH (solid line, Tm = 67 °C) compared with the WT (dashed line, Tm = 48 °C). Data are representative of three independent experiments. The fluorescence intensity (vertical axis) is plotted against the temperature (horizontal axis). (*B*) Overall view of csDH with bound FAD (carbons in yellow). The FAD-binding lobe is in orange and the NADPH-binding lobe in gray. Residues of the C-terminal PW$^{695}$LEL extension are in black. (*C*) NADPH-oxidase activity of the isolated csDH. WT (●) exhibits $k_{cat}$ = 128.5 ± 9.0 min$^{-1}$, $K_m$ = 58.6 ± 11.0 μM, whereas the C-terminally extended mutant (■) shows $k_{cat}$ = 22.8 ± 3.9 min$^{-1}$ and $K_m$ = 165.3 ± 59.5 μM. In this assay, dioxygen is used as the electron-accepting substrate that regenerates the oxidized flavin. The reaction becomes fourfold faster using ferricyanide as electron acceptor ($k_{cat}$ = 261.9 ± 27.7 min$^{-1}$ and $K_m$ = 84.54 ± 22.8 μM). (*D*) The NADPH-binding cleft. NADPH (green carbons) is modeled with the nicotinamide stacking against the isoalloxazine moiety of FAD (yellow carbons) by similarity with spinach ferredoxin-reductase (16). Oxygens are in red, nitrogens in blue, and phosphorous in orange. Phe693, at the C terminus, is in dark gray.

we describe crystal structures of DH and TM, forming the catalytic core common to the whole NOX family. We also describe a mutation of the cytosolic DH that drastically increases its stability in solution and was key to crystallize it. The structural analysis, supported by kinetics and mutagenesis data, presented herein, reveals in unprecedented detail the mechanisms of electron transfer and dioxygen reduction. This structural model considerably advances our understanding of the conformational changes and molecular interactions that orchestrate NOX regulation.

## Results and Discussion

**A Hyperstabilizing Mutation Enabled the Structural Elucidation of NOX's DH Domain.** Purified recombinant *C. stagnale* DH (residues 413–693; csDH) did not retain the FAD cofactor, possibly a symptom of poor protein stability, and crystals did not grow in any of the tested conditions. However, in the course of the protein expression screenings, we serendipitously found that addition of the amino acid sequence PWLELAAA after the C-terminal Phe693 generated a mutant csDH with dramatically enhanced thermal stability (19 °C increase in the unfolding temperature) and FAD retention (Fig. 1*A*). The C-terminal residues are highly conserved (Fig. S1*B*), and the described extension may represent a generally effective way to increase the stability of other NOX enzymes. Crystals of mutant csDH were obtained in vapor-diffusion experiments and the structure solved at 2.2-Å resolution (Table S1). The Trp of the added PW$^{695}$LELAAA positions itself in front of the isoalloxazine ring of FAD with a face-to-face π-stacking interaction (Fig. 1*B* and Fig. S1 *C* and *D*). This Trp–FAD interaction hinders access of the nicotinamide ring of NADP$^+$ to its binding pocket. However, we found that the mutated csDH effectively oxidizes NADPH, albeit with a fivefold slower rate compared with the WT (Fig. 1*C* and Table S2). This observation indicates that the C-terminally added PW$^{695}$LELAAA residues might locally change conformation to allow NADPH-binding. Indeed, in silico docking shows that upon displacement of Trp695, NADPH can easily be modeled to fit in the crevice at the interface of the NADPH- and FAD-binding lobes of DH with the same binding mode observed across the ferredoxin-NADPH reductase superfamily (Fig. 1*D*) (16). On this basis, it can be concluded that our csDH mutant is most likely stabilized in an active conformation, which simply requires the displacement of the C-terminally added residues (i.e., Trp695) to allow NADPH binding and flavin reduction.

The structure of the isolated NADP-binding lobe of human NOX2 is available (PDB ID code 3ALF). As expected, its overall conformation is very similar to that of the same region of csDH. It is of note, however, that there is a large outward shift in the position of the C-terminal residues (up to 7.9 Å for Phe570 of NOX2 compared with the homologous Phe693 of csDH) (Fig. S1*C*). This conformational change might reflect the absence of the FAD-binding domain in the human NOX2 partial structure. Nevertheless, because the superposition of these two structures does not display any structural clash, the shift of the C-terminal Phe also indicates that in NOXs this residue can potentially move inward and outward from the active site.

**NOX DH Domain Contains Structural Features That Are Unique in the Ferredoxin-NADP Oxidoreductase Superfamily.** csDH was further compared with ferrodoxin-NADPH reductases to outline key structural features at the heart of enzyme regulation (Fig. 2 and Fig. S1 *B* and *E*). A first characteristic element is a hairpin within the FAD-binding lobe (Q$^{489}$-G$^{509}$). This segment is longer in human NOX5 than in the other NOX members and binds Hsp90, which is involved in NOX5 stability and activity (17). The other NOX5-specific elements pertain to calcium-regulation, namely two extended segments known to be involved in EF-hand and calmodulin-binding, respectively (18, 19). Upon increase of intracellular $Ca^{2+}$, the N-terminal EF-hand domain binds to and activates NOX5. In the csDH structure, the EF-hand binding loop is unstructured (D$^{611}$-T$^{634}$), probably because of a dynamic role and associated conformational changes that may accompany the enzyme activation. Calmodulin further sensitizes human NOX5 to

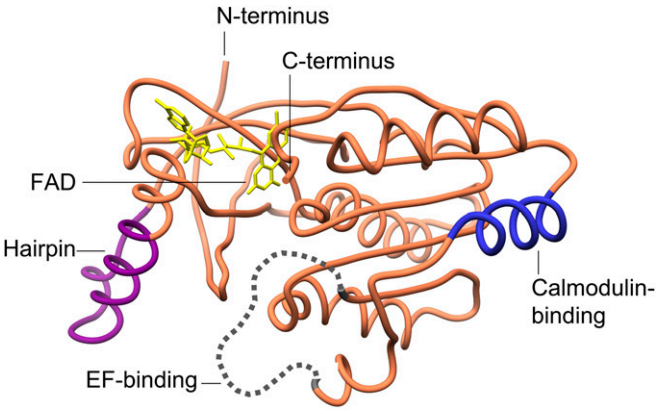


**Fig. 2.** Characteristic structural features of csDH. The domain is depicted in orange with the calmodulin-binding region in blue (R$^{644}$-V$^{663}$) (see Fig. S1*B*), the unstructured EF-hand binding loop in dotted gray (D$^{611}$-T$^{634}$), and the protruding hairpin of the FAD-binding lobe in purple (Q$^{489}$-G$^{509}$).

$Ca^{2+}$ by binding in a region, which, as now shown by the crystal structure, is a solvent-exposed α-helical segment downstream the EF-binding loop ($R^{644}$-$V^{663}$) (Fig. 2 and Fig. S1*E*). Although calmodulin is not found in prokaryotic cells, the conservation of the calmodulin-binding region (37% identity between human and *C. stagnale*) (Fig. S1*B*) may not be merely vestigial, as we cannot exclude the existence of a $Ca^{2+}$-binding protein with similar function to calmodulin in *C. stagnale*. In essence, DH can be described in terms of a typical NADP-ferredoxin oxidoreductase scaffold (16), which is enriched by specific regulatory elements and a mobile C-terminal segment.

**An Uncommon Oxygen-Reacting Center.** The TM domain of csNOX5 (residues 209–412) was crystallized in a lipid mesophase, which provides a better crystallization environment for membrane proteins (20). Because no suitable homology model was available for molecular replacement, we exploited the anomalous signal of the iron atoms bound to the two b-type heme groups (13). The 2.0-Å resolution crystal structure of csTM has an overall pyramidal shape with a triangular base on the inner membrane side and a narrower apex toward the outer membrane face (Table S1). The domain encompasses six transmembrane helices (h1–h6) and an additional N-terminal α-helix, which runs at the surface of and parallel to the inner side of the membrane (Fig. 3 *A*–*C*). The electron density shows the TM to be decorated by four lipid ligands that bind along the helices h1, h3, and h4, and a fifth lipid wedged between the transmembrane helices h1, h2, and h3 (Fig. S2). The two hemes of the transmembrane portion of NOX are positioned with their planes orthogonal to the lipid bilayer in a cavity formed by helices h2, h3, h4, and h5 (Fig. 3*C*). The line connecting their iron atoms is almost exactly perpendicular to the plane of the bilayer (Fig. 3 *A* and *B*). In this way, one heme lies proximal to the cytosolic (inner) side of the domain, whereas the second heme is located toward the outer extracytoplasmic side. The two porphyrins are both hexa-coordinated because they are ligated via two pairs of histidines belonging to helices h3 and h5 (Fig. 3 *D* and *E*). Reduction with dithionite leads to a red shift of the Soret γ-band from 414 nm to 427 nm, accompanied by an increase of amplitude of the α- (558 nm) and β- (528 nm) bands, which is characteristic of heme hexa-coordination (Fig. 4*A*). Consistently, we could not detect any inhibition by cyanide even at high concentrations, as expected for hexa-coordinated hemes (Fig. 4*B*) (21, 22).

We analyzed the csTM structure to model a plausible route for electron passage across the two hemes. The metal-to-metal distance is 19.8 Å, whereas the shortest interatomic distance (6.4 Å) is between vinyl 2 of the inner heme and vinyl 4 of the outer heme (Fischer nomenclature). A cluster of hydrophobic residues (Met306, Phe348, Trp378) intercalates between the two prosthetic groups; of those, the Trp378 indole is within Van der Waals contact distance from both porphyrins (Fig. 5 *A* and *B*). Based on these observations, we hypothesize that a favorite route for electron transfer can be from vinyl 2 of the inner heme via Trp378 to vinyl 4 of the outer heme. The electron is then finally transferred to a dioxygen molecule. In this regard, inspection of the csTM structure reveals an intriguing feature: a small cavity is

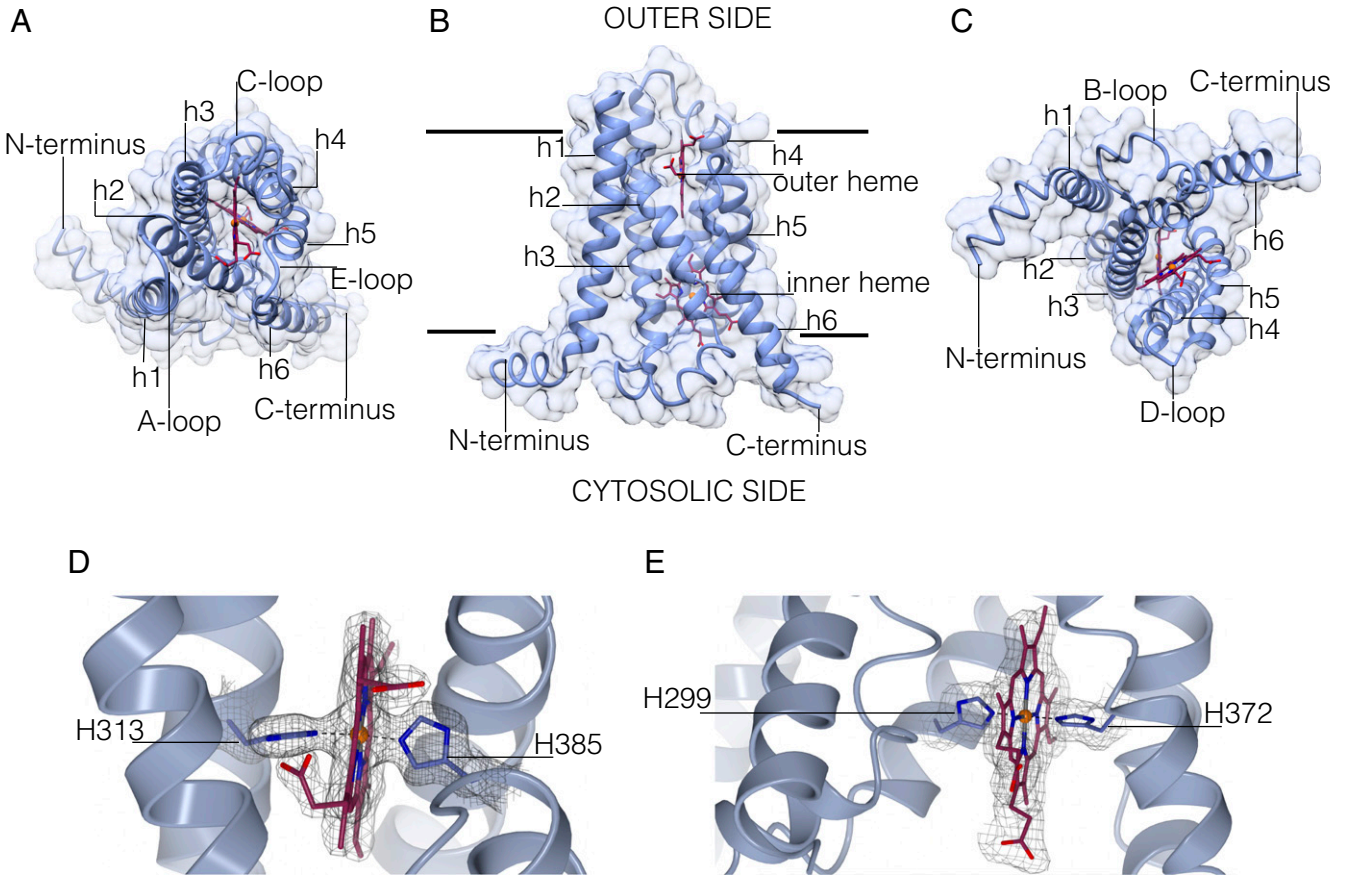


**Fig. 3.** TM of NOX consists of six transmembrane helices and contains two heme groups positioned almost orthogonally to the lipid bilayer. (*A*–*C*) Overall structure of csTM depicted in different orientations (outer, side, and cytosolic view). Transmembrane helices are labeled sequentially as h1–h6. (*D* and *E*) Crystallographic data outline the hexa-coordinated nature of the outer and inner heme groups, respectively. The weighted $2F_o$–$F_c$ electron density maps are contoured at 1.4 σ levels.

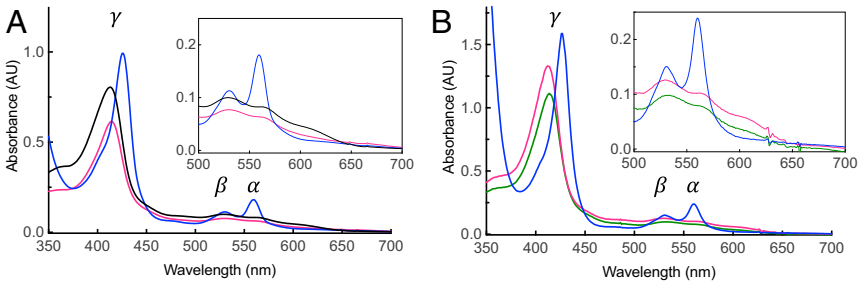


**Fig. 4.** UV/visible absorption spectra of native and reduced csTM domain support the hexa-coordinated nature of heme binding to NOX5. (*A*) Spectra of purified csTM alone (anaerobiosis; black) reduced with dithionite (blue) and reoxidized with dioxygen (purple). (*B*) csTM does not react with cyanide. Spectra of purified csTM incubated first with 1 mM potassium cyanide (green), then with 10 mM dithionite (blue), and reoxidized with dioxygen (purple). *Insets* show expanded spectra in the range between 500 and 700 nm.

located above the outer heme and occupied by a highly ordered water molecule (Fig. 5*C*). This cavity is lined by the propionate 7 of the heme (Fisher nomenclature) and the strictly conserved residues Arg256, His317, and iron-coordinating His313. Many features indicate that the cavity-bound water molecule actually occupies the position of the dioxygen substrate. Its H-bonding environment is clearly suited for $O_2$ binding and sequestration (Fig. 5*D*). Moreover, the positive charge of Arg256 can electrostatically promote the catalytic production of superoxide, as observed in other oxygen-reacting enzymes (23, 24). In agreement with the notion that the site lined by Arg256 and His317 is involved in $O_2$ binding and catalysis, we found that reoxidation of chemically reduced csTM is greatly impaired by mutations targeting these two residues (Fig. 5 *C* and *D*). Rapid kinetics experiments show that

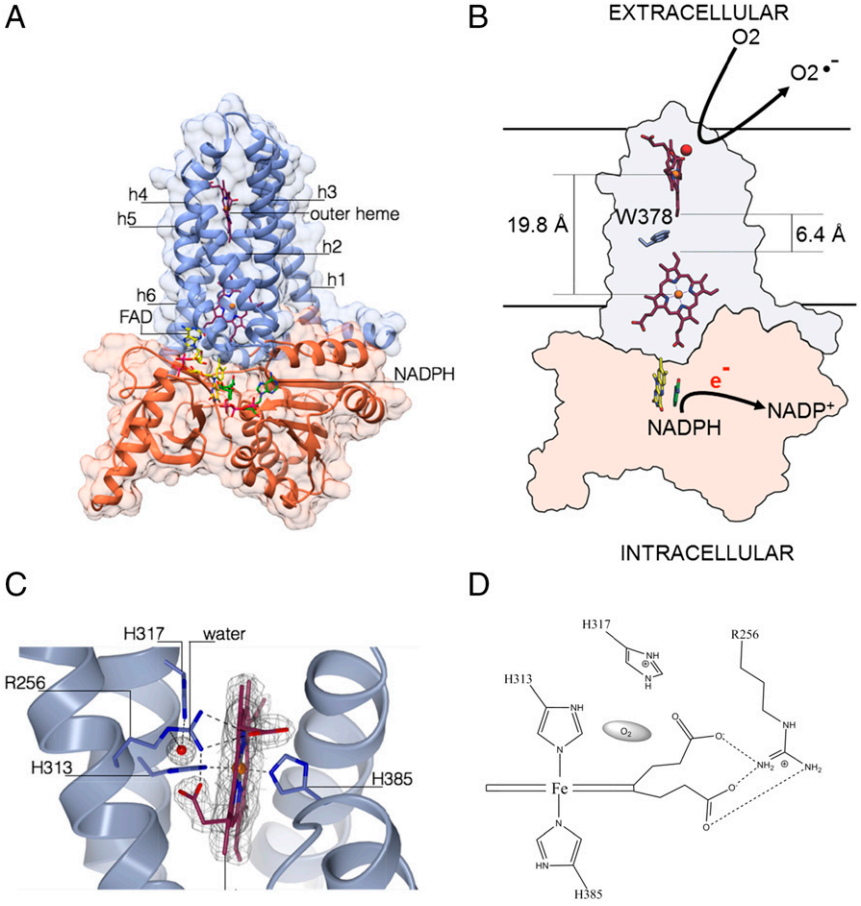


**Fig. 5.** A model for the TM–DH core of NOX catalytic subunit as gathered from the crystal structures of DH and TM domains from csNOX5. (*A*) The in silico docking of csTM (light blue) and csDH (orange) structures is shown in a putative active conformation (see Fig. S4 and *SI Materials and Methods* for details). (*B*) A distance of 19.8 Å separates the metal centers of the two heme groups of TM. Electron transfer may follow a path through Trp378. This residue corresponds to a Val362 in human NOX5 (but the adjacent Trp363 may also offer a suitable route), Phe215 in human NOX2, and Phe200 in human NOX4 (Fig. S1*B* and Table S5). (*C*) A highly ordered water molecule is present in a cavity lined by the outer heme at 3.8 Å distance from the iron (Fig. 3 *A*–*C*) and exposed toward the external milieu, highlighting the oxygen-reacting center. The weighted $2F_o$–$F_c$ electron density map is contoured at 1.4 σ level. (*D*) Schematic view of the cavity with groups putatively interacting with dioxygen.

reduced WT csTM is very quickly oxidized even at low $O_2$ concentration (~300 $s^{-1}$ at 4.5 μM $O_2$). Conversely, the R256S and H317R mutants can be fully reoxidized only at higher $O_2$ concentration (600 μM), with rates at least fivefold lower than observed for WT csTM (Fig. S3 and Table S3). Notably, whereas the R256S mutant displayed the same apparent melting temperature (Tm) as the WT (61 °C), the H317R variant showed lower protein stability (appTm = 43.5 °C) (Table S4). The functional importance of Arg256 and His317 is further documented by disease-inducing mutations affecting the corresponding residues of human NOX2. These mutations were shown to impair catalytic activity (25–27), but until now no mechanistic explanation could be provided (for an extended analysis of NOX2 mutations, see Fig. S4*A* and Table S5).

These findings have far-reaching implications for our understanding of the chemical mechanism of ROS generation. Dioxygen binding does not appear to occur through direct coordination to the iron of the heme, which is in a hexa-coordinated state (Fig. 5*C*). Rather, dioxygen interacts noncovalently with the prosthetic group and surrounding hydrophilic side chains. This observation implies that superoxide formation does not happen through an innersphere mechanism, which is brought about by the oxygen directly coordinating to the iron as, for example, in the globin class of hemoproteins (28). It is instead an outersphere reaction that affords reduction of molecular oxygen through an electron transfer step, as originally suggested by Isogai et al. (29). This may occur either by direct contact between the reduced heme and $O_2$ or be mediated by the iron-coordinating His313 side chain.

**A Structural Framework for NOX Catalysis and Regulation.** With the insight gained from the individual DH and TM domains, we next addressed the issue of their assembly to model the NOX catalytic core. A first noteworthy observation is that the surface on the inner side of TM is remarkably complementary in shape to the bilobal surface of DH, where the flavin ring is exposed (Fig. 5 *A* and *B* and Fig. S4 *B* and *C*). Furthermore, the C terminus of the csTM structure (residue 412) must necessarily be close in space to the N terminus of csDH (residue 413). On these bases, the two domain structures were computationally docked to generate a full TM–DH complex (see *SI Materials and Methods* for details). This model corresponds to the epsilon splicing isoform of human NOX5, which lacks the regulatory N-terminal EF-hand domain (30). Of relevance, the catalytic subunits of the oligomeric NOX1–4 also consist only of DH–TM with no other domains (14). Therefore, the general functional and catalytic implications of our analysis are likely to be relevant to the whole NOX family.

A first point outlined by the TM–DH model is that the flavin is positioned with its exposed dimethylbenzene ring in direct contact with the TM's inner heme (the propionate chains in particular) (Fig. 5*B*). This geometry is obviously suited to promote the interdomain electron transfer that injects the NADPH-donated electrons from the flavin to the heme-Trp378-heme array. Another critical observation concerns the extensive interdomain interactions involving the C-terminal residues of DH and the loops connecting helices h2–h3 and h4–h5 of TM (known as B and D loops, respectively) (Fig. 3*C* and Fig. S1*B*). In NOX4 and NOX2, these loops were shown to contribute to the regulation of the enzyme activity (31, 32). Of note, our structural model positions the TM's B-loop in direct interaction with a highly conserved α-helix/β-strand element of DH (Fig. S5). These residues ($L^{507}$-$L^{533}$) are part of the B-loop interacting region as reported for NOX2 and -4 based on peptide-binding experiments (Fig. S1*B*) (31). Moreover, Arg360 and Lys361 on loop D are modeled in direct contact with the C-terminal Phe693 of DH, in the core of the nicotinamide-binding site (Fig. S4 *B* and *C*). This arrangement is fully consistent with published data demonstrating that both loops contribute to the ROS-producing activity and its regulation in NOX2/4 (31, 32).

The elucidation of NOX 3D structure outlines a general scheme for NOX regulation with the C-terminal residues functioning as regulatory toggle switch. A mobile C-terminal segment is hinted by the above-discussed structural comparisons between the NADPH-binding lobes of csDH and human NOX2 (Fig. S1*C*). Notably, an aromatic C-terminal residue (i.e., Phe693 in csNOX5) is widespread among NADP-ferredoxin reductases, where it is often found to change its conformation depending on NADPH-binding (16). The substitution Phe693Ser showed a twofold increase in $V_{max}$ compared with the WT, whereas the deletion of Phe693 did not elicit any remarkable change on the steady-state kinetic properties of the DH domain (Table S2). This observation implies that Phe693 has a limited influence on the catalysis of the isolated DH domain, which is in a deregulated active state. Rather, the regulatory role of strictly conserved Phe693 is predicted to emerge only in the context of the full-length protein. Phe693 and nearby C-terminal residues may function as a receiver that conformationally transduces inhibitory or activating signals from other regulatory domains or subunits. For example, in the case of NOX5, the regulatory calmodulin- and EF-hand binding segments are located in proximity of the C-terminal residues and NADPH-binding site (Fig. 2). It can be envisioned that $Ca^{2+}$-dependent activation may entail the binding of EF-hand and calmodulin to their respective receiving loops, thereby promoting the NADPH-binding conformation of the nearby residues (Fig. S6). It can also be hypothesized that these conformational changes further promote the attainment of the competent redox-transfer conformation at the flavin–heme interface where the D-loop is located (Fig. S6). Given the high conservation of the C-terminal residues, similar mechanisms to convey regulatory signals to the catalytic core might be operational also in other NOXs (33, 34) (Fig. S1*B*). Of interest, an allosteric mechanism of enzyme regulation involving NADH-binding has been recently found also in the flavoenzyme apoptosis-inducing factor (35). The crucial feature of this mechanistic proposal is that NADPH-oxidation at the flavin site takes place only when the enzyme is in the active conformation, thus preventing the risk of NADPH-derived electrons being diverted to nonproductive redox reactions.

The powerful production (or its deregulation/deficiency) of ROS by NOXs underlies pathological conditions, such as oxidative stress, malignancies, neurodegenerative disease, senescence, and chronic granulomatous disease (1–12) (Fig. S4*A* and Table S5). Our results highlight key structural elements common to the entire NOX family, such as the toggle-switch at the C terminus and the dioxygen binding pocket. The NOX structural model presented here and its analysis bear strong implications for the design of drugs targeting the NOX family.

## Materials and Methods

Protein expression, purification, mutant preparation, and enzymatic assays are described in *SI Materials and Methods*. Initial crystallization experiments on the csDH and csDH-PWLELAAA were carried out at 20 °C using Oryx8 robot (Douglas Instruments) and sitting-drop vapor-diffusion technique. The drops were composed of 0.2 μL of 7 mg/mL protein in 50 mM Tris·HCl pH 7.5, 5% (vol/vol) glycerol, and 0.2 μL of reservoir from commercial screens (JCGS core suite I, II, III, and IV from Qiagen). Crystals of csDH-PWLELAAA grew overnight in two different conditions: (*i*) 160 mM Ca-acetate, 80 mM Na-Cacodylate pH 6.5, 14% (wt/vol) PEG 8000, 20% (vol/vol) glycerol; and (*ii*) 100 mM CHES pH 9.5, 40% (vol/vol) PEG 600. Crystals used for data collection were obtained using a reservoir consisting of 160 mM Ca-acetate, 80 mM Na-Cacodylate pH 6.5, 12–16% (wt/vol) PEG 8000, 20% (vol/vol) glycerol. csTM was concentrated to 25 mg/mL and mixed with monoolein (1-oleoyl-rac-glycerol) in a 2:3 protein to lipid ratio (wt/wt) using two coupled syringes (Hamilton) at 20 °C. The in *meso* mix was dispensed manually using a Hamilton syringe coupled to a repetitive dispenser onto a sandwich plate in a 120-nL bolus overlaid by 1 μL of precipitant solution. Red csTM crystals grew in 2 d at 20 °C in 30% (vol/vol) PEG300, 100 mM $Li_2SO_4$, 100 mM Mes-KOH pH 6.5.

csDH crystals were harvested and flash-frozen in liquid nitrogen. Data were measured at 100 K at beam-lines in the Swiss Light Source (Villigen, Switzerland) and European Synchrotron Radiation Facility (Grenoble, France). Data were indexed and integrated with XDS (36) and scaled with aimless (CCP4suite) (37). The structure of csDH was solved by molecular replacement using Balbes (37). Initial amino acid placement was carried out using phenix.autobuild (38) and checked by Coot. Refinement at 2.0 Å was done by iterative cycles of Refmac5 (37) and Coot (39). Datasets for the csTM were collected at European Synchrotron Radiation Facility (Grenoble, France), Swiss Light Source (Villigen, Switzerland), and Deutsches Elektronen-Synchrotron (Hamburg, Germany). They were processed with XDS (36) and scaled with aimless (37). The initial phases were obtained by iron-based single-wavelength anomalous dispersion using the program autoSHARP (40). Two iron sites were identified and a crude helical model was built by phenix.autobuild. Phases were recalculated on the native dataset using DMMULTI (41). The model was further improved with iterative cycles of coot, phenix.fem and Refmac5 (38, 39). Images were prepared using Chimera (42) and CCP4MG (37). Electron flow trajectory was calculated with VMD Pathways1.1 plug-in (43).

**ACKNOWLEDGMENTS.** We thank the Swiss Light Source, European Synchrotron Radiation Facility, and Deutsches Elektronen-Synchrotron for providing synchrotron radiation facilities, and their staff for supervising data collection; Stefano Rovida and Federico Forneris for providing technical support with inhibition assays and crystallographic analyses; Thomas Schneider (European Molecular Biology Laboratory–Deutsches Elektronen-Synchrotron, Hamburg) for his help and assistance; and Claudia Binda and Federico Forneris for critical reading of the manuscript. Research in the authors' laboratory is supported by the Associazione Italiana per la Ricerca sul Cancro (IG-15208) and the Italian Ministry for University and Research (PRIN2015-20152TE5PK_004). X-ray diffraction experiments were supported by the European Community's Seventh Framework Programme (FP7/2007-2013) under BioStruct-X (Grants 7551 and 10205).

1. Bedard K, Krause KH (2007) The NOX family of ROS-generating NADPH oxidases: Physiology and pathophysiology. *Physiol Rev* 87:245–313.
2. Lambeth JD, Neish AS (2014) Nox enzymes and new thinking on reactive oxygen: A double-edged sword revisited. *Annu Rev Pathol* 9:119–145.
3. O'Neill S, Brault J, Stasia MJ, Knaus UG (2015) Genetic disorders coupled to ROS deficiency. *Redox Biol* 6:135–156.
4. Sirokmány G, Donkó Á, Geiszt M (2016) Nox/Duox family of NADPH oxidases: Lessons from knockout mouse models. *Trends Pharmacol Sci* 37:318–327.
5. Drummond GR, Selemidis S, Griendling KK, Sobey CG (2011) Combating oxidative stress in vascular disease: NADPH oxidases as therapeutic targets. *Nat Rev Drug Discov* 10:453–471.
6. Kuroda J, et al. (2010) NADPH oxidase 4 (Nox4) is a major source of oxidative stress in the failing heart. *Proc Natl Acad Sci USA* 107:15565–15570.
7. Gao HM, Zhou H, Hong JS (2012) NADPH oxidases: Novel therapeutic targets for neurodegenerative diseases. *Trends Pharmacol Sci* 33:295–303.
8. Hoste C, Rigutto S, Van Vliet G, Miot F, De Deken X (2010) Compound heterozygosity for a novel hemizygous missense mutation and a partial deletion affecting the catalytic core of the $H_2O_2$-generating enzyme DUOX2 associated with transient congenital hypothyroidism. *Hum Mutat* 31:E1304–E1319.
9. Block K, Gorin Y (2012) Aiding and abetting roles of NOX oxidases in cellular transformation. *Nat Rev Cancer* 12:627–637.
10. Weyemi U, et al. (2012) ROS-generating NADPH oxidase NOX4 is a critical mediator in oncogenic H-Ras-induced DNA damage and subsequent senescence. *Oncogene* 31:1117–1129.
11. Ogrunc M, et al. (2014) Oncogene-induced reactive oxygen species fuel hyperproliferation and DNA damage response activation. *Cell Death Differ* 21:998–1012.
12. Teixeira G, et al. (June 7, 2016) Therapeutic potential of NADPH oxidase 1/4 inhibitors. *Br J Pharmacol*, 10.1111/bph.13532.
13. Finegold AA, Shatwell KP, Segal AW, Klausner RD, Dancis A (1996) Intramembrane bis-heme motif for transmembrane electron transport conserved in a yeast iron reductase and the human NADPH oxidase. *J Biol Chem* 271:31021–31024.
14. Zhang X, Krause KH, Xenarios I, Soldati T, Boeckmann B (2013) Evolution of the ferric reductase domain (FRD) superfamily: Modularity, functional diversification, and signature motifs. *PLoS One* 8:e58126.
15. Cheng G, Cao Z, Xu X, van Meir EG, Lambeth JD (2001) Homologs of gp91phox: Cloning and tissue expression of Nox3, Nox4, and Nox5. *Gene* 269:131–140.
16. Deng Z, et al. (1999) A productive $NADP^+$ binding mode of ferredoxin-$NADP^+$ reductase revealed by protein engineering and crystallographic studies. *Nat Struct Biol* 6:847–853.
17. Chen F, et al. (2015) Nox5 stability and superoxide production is regulated by C-terminal binding of Hsp90 and CO-chaperones. *Free Radic Biol Med* 89:793–805.
18. Tirone F, Radu L, Craescu CT, Cox JA (2010) Identification of the binding site for the regulatory calcium-binding domain in the catalytic domain of NOX5. *Biochemistry* 49:761–771.
19. Tirone F, Cox JA (2007) NADPH oxidase 5 (NOX5) interacts with and is regulated by calmodulin. *FEBS Lett* 581:1202–1208.
20. Caffrey M (2015) A comprehensive review of the lipid cubic phase or in meso method for crystallizing membrane and soluble proteins and complexes. *Acta Crystallogr F Struct Biol Commun* 71:3–18.
21. Iizuka T, Kanegasaki S, Makino R, Tanaka T, Ishimura Y (1985) Studies on neutrophil b-type cytochrome in situ by low temperature absorption spectroscopy. *J Biol Chem* 260:12049–12053.
22. Miki T, Fujii H, Kakinuma K (1992) EPR signals of cytochrome b558 purified from porcine neutrophils. *J Biol Chem* 267:19673–19675.
23. Mattevi A (2006) To be or not to be an oxidase: Challenging the oxygen reactivity of flavoenzymes. *Trends Biochem Sci* 31:276–283.
24. Shin DS, et al. (2009) Superoxide dismutase from the eukaryotic thermophile *Alvinella pompejana*: Structures, stability, mechanism, and insights into amyotrophic lateral sclerosis. *J Mol Biol* 385:1534–1555.
25. Cross AR, Heyworth PG, Rae J, Curnutte JT (1995) A variant X-linked chronic granulomatous disease patient (X91+) with partially functional cytochrome b. *J Biol Chem* 270:8194–8200.
26. Rae J, et al. (1998) X-Linked chronic granulomatous disease: Mutations in the CYBB gene encoding the gp91-phox component of respiratory-burst oxidase. *Am J Hum Genet* 62:1320–1331.
27. Picciocchi A, et al. (2011) Role of putative second transmembrane region of Nox2 protein in the structural stability and electron transfer of the phagocytic NADPH oxidase. *J Biol Chem* 286:28357–28369.
28. Shikama K (1998) The molecular mechanism of autoxidation for myoglobin and hemoglobin: A venerable puzzle. *Chem Rev* 98:1357–1374.
29. Isogai Y, Iizuka T, Shiro Y (1995) The mechanism of electron donation to molecular oxygen by phagocytic cytochrome b558. *J Biol Chem* 270:7853–7857.
30. Fulton DJ (2009) Nox5 and the regulation of cellular function. *Antioxid Redox Signal* 11:2443–2452.
31. Jackson HM, Kawahara T, Nisimoto Y, Smith SM, Lambeth JD (2010) Nox4 B-loop creates an interface between the transmembrane and dehydrogenase domains. *J Biol Chem* 285:10281–10290.
32. Carrichon L, et al. (2011) Characterization of superoxide overproduction by the D-Loop(Nox4)-Nox2 cytochrome b(558) in phagocytes—Differential sensitivity to calcium and phosphorylation events. *Biochim Biophys Acta* 1808:78–90.
33. Rotrosen D, Yeung CL, Leto TL, Malech HL, Kwong CH (1992) Cytochrome b558: The flavin-binding component of the phagocyte NADPH oxidase. *Science* 256:1459–1462.
34. Dahan I, Molshanski-Mor S, Pick E (2012) Inhibition of NADPH oxidase activation by peptides mapping within the dehydrogenase region of Nox2-A "peptide walking" study. *J Leukoc Biol* 91:501–515.
35. Brosey CA, et al. (2016) Defining NADH-driven allostery regulating apoptosis-inducing factor. *Structure* 24:2067–2079.
36. Kabsch W (2010) XDS. *Acta Crystallogr D Biol Crystallogr* 66:125–132.
37. Winn MD, et al. (2011) Overview of the CCP4 suite and current developments. *Acta Crystallogr D Biol Crystallogr* 67:235–242.
38. Adams PD, et al. (2010) PHENIX: A comprehensive Python-based system for macromolecular structure solution. *Acta Crystallogr D Biol Crystallogr* 66:213–221.
39. Emsley P, Cowtan K (2004) Coot: Model-building tools for molecular graphics. *Acta Crystallogr D Biol Crystallogr* 60:2126–2132.
40. Vonrhein C, Blanc E, Roversi P, Bricogne G (2007) Automated structure solution with autoSHARP. *Methods Mol Biol* 364:215–230.
41. Cowtan KD (1994) DM: An automated procedure for phase improvement by density modification. *Joint CCP4 and ESF-EACBM Newsletter on Protein Crystallography* 31:34–38.
42. Pettersen EF, et al. (2004) UCSF Chimera—A visualization system for exploratory research and analysis. *J Comput Chem* 25:1605–1612.
43. Balabin IA, Hu X, Beratan DN (2012) Exploring biological electron transfer pathway dynamics with the Pathways plugin for VMD. *J Comput Chem* 33:906–910.
44. van Zundert GC, et al. (2016) The HADDOCK2.2 Web Server: User-friendly integrative modeling of biomolecular complexes. *J Mol Biol* 428:720–725.
45. Lensink MF, et al. (2016) Prediction of homoprotein and heteroprotein complexes by protein docking and template-based modeling: A CASP-CAPRI experiment. *Proteins* 84:323–348.
46. Piirilä H, Väliaho J, Vihinen M (2006) Immunodeficiency mutation databases (IDbases). *Hum Mutat* 27:1200–1208.